RSC Advances

ROYAL SOCIETY OF CHEMISTRY

www.rsc.org/advances

A table of content entry

Sb-rich Sb_2Se_3 with hollow sphere morphology presents efficient catalysis for the hydrogenation of *p*-nitrophenol.

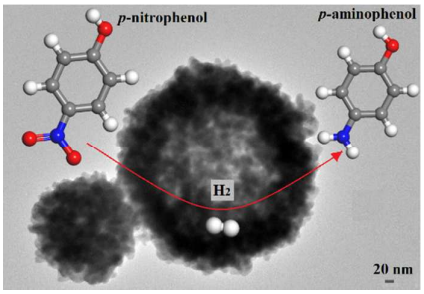

RSC Advances

RSCPublishing

PAPER

Morphology control of Sb-rich Sb_2Se_3 for adjusting the catalytic hydrogenation property of *p*-nitrophenol

Cite this: DOI: 10.1039/x0xx00000x

A.D. Tang,* M. Long, P. Liu, L. Tan and Z. He

Received 24th September 2014,
Accepted 00th October 2014

DOI: 10.1039/x0xx00000x

www.rsc.org/

Sb-rich Sb_2Se_3 with hollow spherical morphology and Se-rich Sb_2Se_3 with rod-like shape were prepared by hydrothermal method using sodium borohydride as the reductant. It is found that the material with high Sb content and microsphere-like morphology presents efficient catalytic performance for the hydrogenation of *p*-nitrophenol. Systematic study on the effect of hydrothermal-reaction time for controlling the structure and morphology of Sb-rich Sb_2Se_3 shows that the products mainly composed of rod-like and hollow sphere-like Sb_2Se_3 under the different conditions, and the microsphere particles are mainly composed of Sb and Sb_2Se_3 while the rod-like particles are made of Se-rich Sb_2Se_3. The longer hydrothermal reaction duration with the Sb/Se atomic ratio of 1:1.2 could cause the increase of the amount of spherical Sb-rich Sb_2Se_3 particles, which showed the enhanced catalytic activity. It is found that hollow spherical Sb-rich Sb_2Se_3 exhibits much better catalytic performance than the rod-shaped Se-rich Sb_2Se_3, which may be attributed to the higher dispersity of antimony and the small size of the hollow spherical morphology of Sb-rich Sb_2Se_3 particles (less than 50 nm). The potential growth mechanism for different morphologies of Sb-rich Sb_2Se_3 has been proposed by analyzing the samples at different growth stages.

1. Introduction

Semiconductors nanostructures have received a great deal of attentions due to their applications in television cameras with photo conducting targets, thermoelectric devices, optoelectronic devices, IR spectroscopy [1-4]. Among these semiconductors, Sb_2Se_3 as a direct band gap semiconductor, has wide-ranging applications in solar selective and decorative coating, excellent photovoltaic properties, and high thermoelectric power, and new application in catalytic reduction[5, 6]. Inspired by its remarkable characteristics, various routes have been developed for the synthesis of Sb_2Se_3 nanomaterials in recent years, such as solvothermal/hydrothermal methods [7, 8], chemical bath deposition [6], gas-induced-reduction method [9], electrochemical method [10] and microwave-assisted method [11, 12]. Among various synthetic methods, the hydrothermal/solvothermal method is one of the most promising routes because of its low growth temperature and effectiveness for fabricating nanoparticles with controlled phases and morphologies, selectively preparing 1D to 3D nanostructures by varying the volume ratio of the mixed solvents [13].

School of Chemistry and Chemical Engineering, Central South University, Changsha, 410083, P.R.China

**Corresponding author, email: tangaidong@126.com; adtang@csu.edu.cn, Tel.: +86-731-88879616, Fax: +86-731-88879616.*

Properties of nanomaterials largely depend on their composition, size and morphology. For instance, urchin-like hierarchical Sb_2Se_3 structures with high electrochemical hydrogen storage [14] and uniform Sb_2Se_3 nanowires for high-performance photo detectors have been fabricated [12]. The Sb_2Se_3 nanowires have potential wide applications in hydrogen storage and high-energy battery [15]. Sb_2Se_3 composed of numerous lamellas with average thickness of circa 10 nm showed efficient catalytic performance for the reduction of *p*-nitrophenol to *p*-aminophenol [1]. However, synthesis and property of Sb-rich Sb_2Se_3 catalyst has not been reported yet. Therefore, the work on organization and design synthesis needs to be developed for more novel properties and applications of antimony chalcogenide nanomaterials.

The catalytic reduction of *p*-nitrophenol to *p*-aminophenol is very meaningful, because *p*-aminophenol has important applications as an analgesic and anti-pyretic drug, such as acetanilide, phenacetin, paracetamol, etc [16, 17]. Although the reduction of high concentration *p*-nitrophenol by zero valent iron system has been realized at the higher operating temperature (85 ^oC)[18], it would be easily proceeded using $NaBH_4$ as the reductant at ambient temperature as a model reaction[1, 19, 20]. Therefore, expensive $NaBH_4$ was selected as the reductant. Recently, the work of developing new nanocatalysts for catalytic reduction of *p*-nitrophenol has aroused a big attention. Among these catalysts, mesoporous Au/TiO_2 nanocomposites[17], Au/graphene hydrogel[21], carbon-protected Au/TiO_2 [22], $Pd@TiO_2$[19] and Fe_3O_4@PS@ PAMA-Ag[23] exhibited excellent catalytic

performance towards the reduction of *p*-nitrophenol to *p*-aminophenol. However, the problem is that there is a high cost due to the usage of noble metal. Therefore, it is highly desirable to develop a new catalyst to replace expensive metal catalysts. Recently, selectively synthesizing Sb_2Se_3 nanostructures represents some exciting progresses. However, rare work has focused on the preparation and performance of Sb-rich Sb_2Se_3 catalyst, whose catalytic properties have not been unveiled thoroughly yet. Herein, we investigated the possibility of reduction of Se powder and $K(SbO)C_4H_4O_6{\cdot}0.5H_2O$ into Sb-rich Sb_2Se_3 in the presence of sodium borohydride under hydrothermal conditions. By simply monitoring the concentrations of the Sb/Se atomic ratio, and hydrothermal reaction time, rod-like and hollow microsphere Sb-rich Sb_2Se_3 can be successfully obtained. Moreover, it is found that Sb-rich Sb_2Se_3 with microsphere-like morphology presents high catalytic performance for the hydrogenation of *p*-nitrophenol. Finally, the possible formation mechanism has been proposed on the basis of a series of XRD, SEM-EDS and TEM characterizations of the products collected at different time intervals.

2. Experimental

2.1 Materials preparation

All of the chemicals were of analytical grade and were used as received. Aqueous solutions were prepared with distilled water. In a typical synthesis, firstly, 0.334g (1mmol) of antimony potassium tartrate $K(SbO)C_4H_4O_6{\cdot}0.5H_2O$ and 0.2g CTAB were dissolved to 20 mL of distilled water, then was heated at 50 ºC under constant stirring until getting a clear colorless solution. Secondly, 0.118 g (1.5mmol) of Se powders were mixed with 10 mL of alcohol (50 vol. %), then 0.113 g (3mmol) of sodium borohydride were added under constant stirring until obtaining a clear colorless solution. Thirdly, dark red brown liquid was obtained by mixing the above two types of clear solution, and gradually changed into black solution by magnetic at 25 ºC for stirring 25 min. Subsequently, the resulting black solution was transferred into an 80 mL Teflon-lined autoclave and 30 mL distilled water was added. Then, the autoclave was sealed, heated, and maintained at 180 °C for 5 h. After the reaction was completed, the product was filtered, washed with distilled water and ethanol absolute three times, and then dried in an oven at 80 °C for 5 h.

2.2 Characterization

X-ray diffraction (XRD) patterns of the products were collected on a Rigaku 2500 X-ray diffractometer at a scanning rate of 0.05 º s^{-1} with a 2θ range from 10 º to 80 º, using high-intensity Cu Kα radiation (λ= 0.15418 nm). The applied current and voltage were 40 mA and 40 kV, respectively. The composition of sample was analyzed by software MDI Jade6. Scanning electron microscope (SEM) images and energy dispersed X-ray spectra (EDS) were obtained on a FEI Nova NanoSEM 230 field emission scanning electron microscope. Microstructures and morphologies were investigated using Tecnai G^2 F20 S-TWIN (FEI Company) transmission electron microscopy (TEM) with a field emission gun of 200 kV. Nitrogen adsorption/desorption isotherms were measured at 77 K by using a Micromeritics ASAP Tristar II 3020 system. The samples were degassed at 453 K overnight on a vacuum line. The Brunauer – Emmett – Teller (BET) method was utilized to calculate the specific surface areas.

2.3 Catalytic activity of *p*-nitrophenol

To test the catalytic activities of the as-prepared Sb_2Se_3 samples, the catalytic reduction of *p*-nitrophenol to *p*-aminophenol (Eq. (1)) was employed as a model reaction[1]. Hydrogen was from an excess amount of $NaBH_4$ (Eq. (2)).

p-nitrophenol+ $3H_2$ → *p*-aminophenol+ $2H_2O$ (1)

$NaBH_4$+ $2H_2O$ → $4H_2$ + $NaBO_2$ (2)

In a typical process, 0.6 mL 0.005 mol/L *p*-nitrophenol solution, 20.0 mL distilled water, and 10.0 mL 0.1 mol/L freshly prepared $NaBH_4$ aqueous solution were added into the beaker in sequence. The solution color turned to bright yellow rapidly, indicating the formation of *p*-nitrophenol ions[1]. Subsequently, 20.0 mg of the as-prepared Sb_2Se_3 was added to the solution kept at 30°C. The changes of the absorbance of *p*-nitrophenol ions were monitored by measuring the maximal absorption at λ =400 nm using a 722s visible spectrophotometer at scheduled time. The rate constant of the reaction was determined by measuring the change of the absorbance at 400 nm as a function of time.

3. Results and discussion

3.1 Structure, morphology and property of Sb_2Se_3 prepared with different Sb/Se atomic ratios

The crystal structures of the resulting products are confirmed by XRD in Fig. 1(a). All of the diffraction peaks can be indexed to orthorhombic phase of Sb_2Se_3 (JCPDS No.04-004-7471), indicating that the as-synthesized Sb_2Se_3 was well crystallized. Meanwhile, one tiny peak originated from Se or Sb can be observed, indicating that the products were mixture consisting Sb_2Se_3 and Se or Sb. When the Sb/Se ratio is 1:1.5, the obtained sample exhibits well crystallinity and orthorhombic structure of Sb_2Se_3 phase with (212) preferred orientation. The tiny peak of Se is weak, which indicates that a small amount of Se still don't react with Sb. When the Sb/Se atomic ratio is increased to 1:1.3 and 1:1.2, the content of antimony in the starting materials is more than the stoichiometric proportion of Sb_2Se_3.

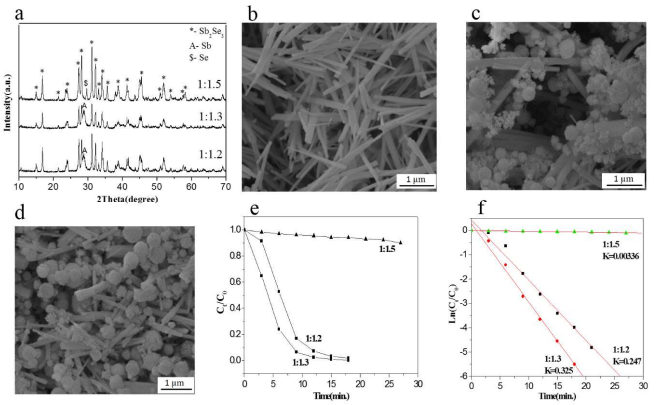

Fig. 1 XRD patterns (a) and SEM images of the products at different ratio of Sb/Se (b)1:1.5; (c)1:1.3; (d)1:1.2 for 5 h hydrothermal reaction; Plot of (e) (c_t/c_0) versus reaction time and (f) $\ln(c_t/c_0)$ versus reaction time in the presence of the Sb_2Se_3 at different the atomic ratios of Sb/Se.

Therefore, it is reasonable that there are peaks of Sb in the Sb_2Se_3 products. It is indicative that the Sb-rich Sb_2Se_3 can be obtained by adjusting the Sb/Se atomic ratio.

The morphologies of samples significantly depend on the Sb/Se ratio, as shown in Fig. 1(b-d). When the Sb/Se ratio is 1:1.5, the nanocrystal growth kinetics significantly depends on their intrinsic crystal structure[7]. Thus, one dimensional rod-like morphology is preferred. It can be found in Fig. 1(b) that the surface of regular rod-like morphology Sb_2Se_3 is smooth and the diameter and length of the rod are about 100-250 nm and 5-8μm, respectively. When the Sb/Se atomic ratio was increased to 1:1.3, the rod significantly grew up. Some mircrospheres appeared with many irregular nanoparticles simultaneously, as can be seen in Fig. 1(c). The obtained microrods show the diameter and length of about 100-300 nm and 3-5 μm, respectively. The average particle size of the microsphere is about 150 nm. Further increasing the Sb/Se atomic ratio to 1:1.2, more mircrospheres with average size of 300 nm can be observed simultaneously, co-existing short microrods with a diameter and length of about 300 nm and 2-4 μm (Fig. 1(d)). It is found that the Sb/Se atomic ratio plays a crucial role in the morphology of Sb_2Se_3.

As a nanostructured material, antimony triselenide is expected to perform excellent catalytical hydrogenation properties. Fig. 1(e) displays the catalytic hydrogenation properties of Sb_2Se_3 nanostructures prepared with different Sb/Se atomic ratios. The catalytic characteristics of the as-prepared Sb_2Se_3 samples are evaluated by the reduction reaction of *p*-nitrophenol to *p*-aminophenol in the presence of excess freshly prepared $NaBH_4$. Fig. 1(e) shows the time-dependent absorbance for a typical reduction process using the Sb_2Se_3 samples prepared with different Sb/Se atomic ratios. The sample prepared with Sb/Se atomic ratio of 1:1.3 shows the highest catalytic performance for reduction of *p*-nitrophenol. The conversion efficiency of *p*-nitrophenol within 15 min could reach approximately 98.0%. The sample prepared with Sb/Se atomic ratio of 1:1.5 shows the lowest catalytic activity of only 10.0% within 15 min. The Se attached on the surface Sb_2Se_3 may play a negative role on its catalytic performance. However, further increasing the Sb/Se atomic ratio to 1:1.2, the conversion efficiency of *p*-nitrophenol within 15 min slightly decrease to 96.7%. By contrast, the Sb-rich samples show higher catalytic activity than the rich-Se Sb_2Se_3 sample obtained using Sb/Se atomic ratio of 1:1.5. Because the concentration of $NaBH_4$ largely exceeds that of *p*-nitrophenol,the concentration of $NaBH_4$ could be regarded as a constant during the reaction. Therefore, a pseudo-first-order rate kinetics with regard to the *p*-nitrophenolate anion concentration could be applied for the evaluation of the catalytic rate[1]. The kinetic equation of the catalytic hydrogenation reduction can be expressed as $\ln(c_t/c_0) = -k_a t$, because the absorbance is proportional to the concentration of *p*-nitrophenol ions in this system, where c_0 denotes the initial concentration of *p*-nitrophenol ions, c_t is the concentration of *p*-nitrophenol ions at time *t*, and k_a is the apparent rate constant. Fig. 1(f) shows the plots of $\ln(c_t/c_0)$ versus time for the reduction of *p*- nitrophenol over Sb_2Se_3 catalysts. The calculated rate constants were estimated using the slopes of straight lines in Fig. 1(f). For comparison between Sb_2Se_3 samples, the rate constants are 0.00336 min^{-1} (Sb/Se=1:1.5), 0.325 min^{-1} (Sb/Se=1:1.3), and 0.247 min^{-1} (Sb/Se=1:1.2), respectively. In contrast, the rate constant of the sample prepared with Sb/Se=1:1.3 is ninety-six times as high as that with Sb/Se=1:1.5. The excellent catalytic performance is attributed to subsequently formation of Sb-rich Sb_2Se_3 microsphere particles. To further explore the reason of high catalytic performance of Sb_x/Sb_2Se_3 catalyst toward reduction of *p*-nitrophenol, it is necessary to further investigate the growth mechanism and catalytic performance of Sb-rich Sb_2Se_3.

3.2 Structure, morphology and catalytic property of products prepared at different hydrothermal time

To investigate the growth mechanism of the microspheres and rod-like morphologies of Sb-rich Sb_2Se_3, a time-dependent experiment was carried out. The Sb-rich Sb_2Se_3 samples, obtained at different time intervals with the Sb/Se atomic ratio of 1:1.2 and CTAB (0.2 g), are characterized by XRD patterns and SEM observations. Fig. 2(a) show a series of XRD patterns of the products by varying the reaction time from 1.5 h, 3 h, 5 h, and 10 h at 180 °C while keeping other conditions constant.

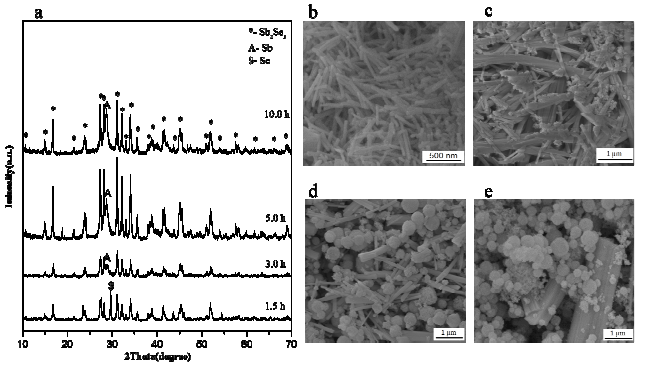

Fig. 2 XRD patterns (a) and SEM images of samples synthesized by a hydrothermal method at 180 °C with the ratio of Sb/Se 1:1.2 for different time intervals (b) 1.5, (c) 3, (d) 5, (e) 10 h.

The presence of Sb_2Se_3 in the samples can be confirmed by the characteristic diffraction peaks at 27.7º, 28.28º, 31.27º and 32.24º, which can be assigned to the (203), (211), (212) and (013) crystal planes of Sb_2Se_3 (JCPDS No.04-004-7471). Meanwhile, one tiny peak originated from Se or Sb also can be observed, as can be seen in Fig. 2(a). At the beginning of 1.5 h, the obtained samples exhibit orthorhombic structure Sb_2Se_3 phase with a strong peak of Se, which indicates that there is more Se produced in 1.5 h to react with the $K(SbO)C_4H_4O_6$. However, the tiny peak of Sb appeared after the hydrothermal reaction carrying out for 3 h and gradually increased with the extended time, indicating that the Sb content increase with the prolonged hydrothermal time. Fig. 2 (b–e) shows the SEM images of the obtained Sb_2Se_3 samples. The corresponding SEM images shown in Fig. 2(b) demonstrate that the product after 1.5 h hydrothermal reaction is composed of uniform rod-

like structures with about 100 nm in diameter and 500 nm in length. For 3 h sample, the rod-like morphology increases with the appearance of irregular nanoparticles in Fig. 2(c). After 5 h of hydrothermal treatment, all the small particles form into sphere-like structures. Microspheres with average size 300 nm could be obtained. The rod-like Sb_2Se_3 continue to increase in Fig. 2(d) simultaneously. Further increasing the hydrothermal reaction time to 10 h, the rod-like morphology is bigger, and sphere-like nanoparticles with sizes about 500 nm become more and more in Fig. 2(e). It means that the extended time leads to over growth of the crystal and produce rod-like and spherical particles with larger diameter.

Table 1 listed the composition, morphology and catalytic activity of nitro-phenol over products prepared with different hydrothermal reaction time. The Reference Intensity Ratio (RIR) is a general, instrument-independent constant for use in quantitative phase analysis by the X-ray powder diffraction internal standard method [24, 25]. The relative content of Sb_2Se_3 and Sb or Se are calculated using the constants collected in the Powder Diffraction File. It is found that the relative content of Sb increases from 5.6 % (hydrothermal time 3 h) to 13.5% (10 h) and the spherical particles are more and more. In addition, the catalytic activity in 15 min from 18.5 % (hydrothermal time 1.5 h) increased up to 96.8% (10 h), similarly, the apparent rate constants also increased from 0.016 min^{-1} (hydrothermal time 1.5 h) to 0.316 min^{-1} (10 h).

Table 1

Summary of the composition, morphology and catalytic activity of nitro-phenol over samples prepared with different hydrothermal reaction time.

t /h	C_{NaBH4} /mmol	Morphology composition */%	Sb phase relative content/ %	$R^{\#}$/%	k_a/min^{-1}
1.5	1.3	R100		18.5	0.016
3	3	R90+S10	5.6	82.5	0.176
5	3	R50+S50	8.3	96.7	0.245
10	3	R40+S60	13.5	96.8	0.316

*: R-rod, S-sphere; morphology percentage is evaluated from Fig. 2(b-e) according to the amount of particles.

$R^{\#}$: Conversion efficiency after reaction 15 min

It could be concluded that the catalytic activity for the reduction of *p*-nitrophenol increased with the hydrothermal time, as indicated from Table 1 and Fig. 1S (a) and (b). The enhanced catalytic performance is attributed to the formation of more sphere-like morphology Sb-rich Sb_2Se_3 particles with increase of Sb content.

3.3 TEM and EDS analysis on the different morphologies of Sb_x/Sb_2Se_3

The TEM and EDS analysis on the different morphologies of the same sample facilitates the understanding of the structure and the composition change of Sb_x/Sb_2Se_3 products. Figure 3 was a representative TEM images and EDS spectrum confirming the composition of the as-prepared sample for rod-like sections collected from 1:1.2 of Sb/Se ratio for hydrothermal reaction 5 h. TEM image (Fig. 3a) clearly reveals that the rod-like product has smooth surface throughout the entire length, possesses an average diameter of ~ 0.5 μm, and a typical length of several micrometres. The high-resolution TEM image (Fig. 3b) and corresponding selected-area electron diffraction (SAED) pattern (Fig. 3c) were acquired from a single rod. The SAED pattern indicates that there are two sets of diffraction spots, indicating that it is two phases appearing on the rod-like product. It is found that there are the Sb_2Se_3 with the (610) growth direction and Sb with the (119) growth direction. The HRTEM further confirm that the interplanar d-spacing of 0.32 nm corresponds to the (112) planes of the orthorhombic Sb_2Se_3 phase, suggesting that the appearance of Sb in the SAED pattern may be the absorption of Sb nanoparticles on the surface of rod-like Sb_2Se_3.

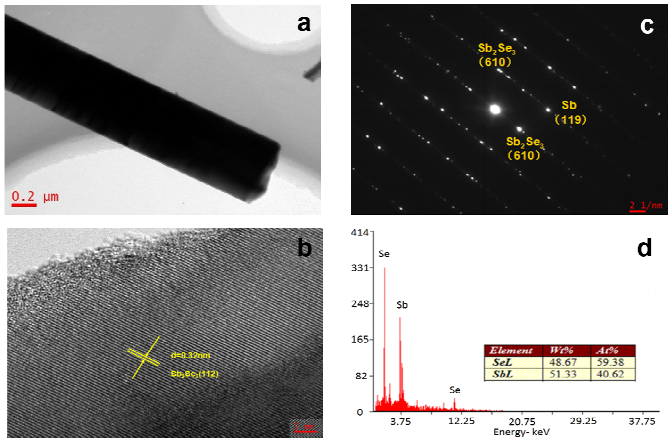

Fig. 3 (a) Typical FESEM image of rod-like Sb_2Se_3 synthesized by hydrothermal method at 180 °C for 5 h, (b) the corresponding SAED pattern of a single Sb_2Se_3 rod, (c) high-resolution TEM image taken from an individual rod, and (d) EDS spectra of rod-like product.

Moreover, the EDS in Fig. 3d reveals strong Sb and Se peaks. The atomic ratio of Sb and Se (40.62:59.38=0.68) is close to the intrinsic 2:3 stoichiometry, confirming the homogeneous purity of the as-prepared Sb_2Se_3. It seems in contradict with the appearance of Sb in Fig. 3(c). Considering that the Sb/Se atomic ratio is 1:1.2, namely, the Sb content is more than the Se content according to the stoichiometric composition of Sb_2Se_3 in the starting materials, additionally not the same site for HRTEM and EDS measurements, one may think that the appearance of Sb on the surface of rod-like Sb_2Se_3 is reasonable.

Figure 4 was a representative TEM image and EDS spectrum confirming the composition of the as-prepared sample for sphere-like sections collected from 1:1.2 of Sb/Se ratio for hydrothermal reaction (5 h). The TEM image (Fig. 4a) clearly reveals that the microsphere is composed of many nanoparticles with size circa of 10-50 nm. The SAED pattern (Fig. 4b) indicates that there is only single phase of Sb with the (116) and (217) diffraction circles on the microsphere nanoparticles, indicating that the size of Sb particle is very small. Furthermore, the high-resolution TEM image (Fig. 4c) further confirms that the interplanar d-spacing of 0.23 nm corresponds to the (104) planes of the Sb phase, suggesting that the surface composition of the microsphere nanoparticles composed of Sb nanoparticles. The distinct enhanced peak of Sb appearing in EDS confirms this viewpoint. The result displayed that the diffraction peaks of

only Sb and Se with different atomic ratio of Sb:Se, 52.40:47.60=1.10 for microsphere (Fig.4d) could be observed.

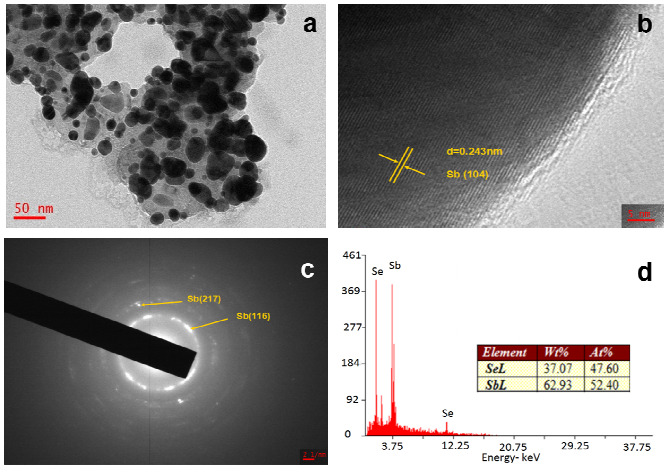

Fig. 4 (a) Typical magnified FESEM image of microsphere particles synthesized by hydrothermal method at 180 °C for 5 h, (b) the corresponding SAED pattern of microsphere particles, (c) high-resolution TEM image taken from a microsphere particle, and (d) EDS spectra of microsphere-like morphology product.

Compared with the rod-like section (Fig.3d), it could be concluded that the atomic compositions of the same sample altered significantly when the samples present different morphology. There is a tendency that the atomic ratio of Sb/Se for rod-like morphology was very close to the stoichiometric composition of the antimony selenide. However, the atomic ratio of Sb/Se (1.10) for microsphere is not only more than that of the rod-like morphology Sb_2Se_3, but also much more than that of Sb/Se (0.83) in the starting materials. The results demonstrate that the microsphere particles are mainly composed of Sb and Sb_2Se_3 while the rod-like particles are made of Se-rich Sb_2Se_3.

3.4 The growth mechanism of Sb-rich Sb_2Se_3

Based on above XRD, SEM/EDS and TEM observations, the Sb/Se atomic ratio of the reactant and the reaction time both have significant effects on the growth and transformation of the Sb_2Se_3 nanoparticles. Firstly, the Se powders were easily reduced into HSe^- ions via sodium borohydride (Eq. (3)), which was not thermodynamic stable in the presence of sodium borohydride. The clear solution changed into red solution in air due to the HSe^- ions easy to be oxidized into Se by oxygen when the solution contacts with air (Eq. (4)). Secondly, when the above clear HSe^- ions solution mixed with the clear $K(SbO)C_4H_4O_6{\cdot}0.5H_2O$ and CTAB solution, the Sb_2Se_3 quickly formed according to Eq. (5). As a result, the rod-like Sb_2Se_3 nuclei were fabricated.

$$Se+NaBH_4+2H_2O \rightarrow NaHSe+HBO_2+3H_2 \quad (3)$$

$$2HSe^-+O_2 \rightarrow 2Se+2OH^- \quad (4)$$

$$2SbO^++3HSe^- \rightarrow Sb_2Se_3+OH^-+H_2O \quad (5)$$

$$2SbO^++NaBH_4 \rightarrow 2Sb+NaBO_2+2H^++H_2 \quad (6)$$

$$2Sb+3Se \rightarrow Sb_2Se_3 \quad (7)$$

In addition, the Se powders were easily reduced into HSe^- ions due to the strong reduction of sodium borohydride, while the SbO^+ ions were relatively difficulty to be reduced to Sb element due to its higher reduction potential. Therefore the rich-Se Sb_2Se_3 could be obtained at the initiate stage. As the reaction time prolonged, the formation of Sb_2Se_3 consumes the reduced HSe^- ions, and the excess Sb formation via Eq. (6) produces H^+, at the same time the formation of nanoparticle Se proceed through the reverse reaction of Eq.(3). Therefore, Sb-rich Sb_2Se_3 microsphere particles produce via Eq. (7) under the hydrothermal reaction[26], which contributes to the repulsive interaction of CTAB of positive charge on SbO^+ ions and Ostwald ripening mechanism. Therefore, due to the strong reductivity of sodium borohydride, the products of Se-rich Sb_2Se_3 quickly form since the relatively fast conversion of Se element to HSe^- ions while relatively slow SbO^+ ions to Sb in the solution at the initial reaction stage, and the supperfluous Sb was produced accompanying appearance of Sb_2Se_3 at the last reaction stage. This is the reason why there is always the elemental Se or Sb appearance with Sb_2Se_3.

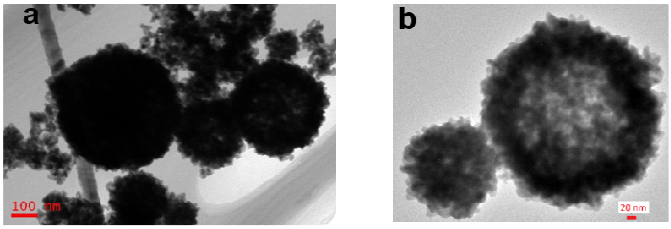

Fig. 5 Typical TEM images of Sb_x/Sb_2Se_3 nanoparticles synthesized by hydrothermal method at 180 °C for (a) 5 h, (b) 10 h.

What's more, the transformation from the poor crystallites of rod-like Sb_2Se_3 to better crystalline rod-like Sb_2Se_3 through Ostwald ripening can be observed as the hydrothermal reaction time prolonged. More importantly, the representative TEM images further reveal that the hollow structure of the microsphere particles growing 5 h and 10 h, respectively (Fig. 5). The hollow microsphere particles (Fig. 5) notably appear as the hydrothermal reaction time prolonged due to the effect of CTAB and the Ostwald ripening mechanism.

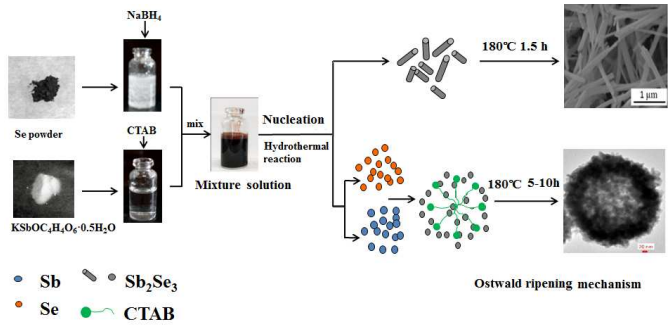

Fig. 6 A schematic illustration of the stepwise preparation process of the rods and hollow microsphere Sb_x/Sb_2Se_3.

Therefore, the hydrothermal reaction mechanism of rod-like Se-rich Sb_2Se_3 and hollow microsphere-like Sb-rich Sb_2Se_3 could be explained as follow Fig. 6 and Eq. (3)–(7). The formations

of rod-like Se-rich Sb_2Se_3 and hollow microsphere-like Sb-rich Sb_2Se_3 follow different growth mechanism under the hydrothermal condition using sodium borohydride as reductant.

The as-prepared Sb_2Se_3 with enriched Sb products show more efficient catalytic performance, which is about 96 times larger than Se-rich Sb_2Se_3 for reduction of *p*-nitrophenol to *p*-aminophenol at room temperature as shown in Fig. 1(f). In addition, it exhibited comparable catalytic performance with the previously reported values for Sb_2Se_3 with lamellar nanostructures[1]. The N_2 adsorption–desorption isotherms of two samples are shown in Fig. S2 for comparing the specific surface areas of Sb-rich Sb_2Se_3 and Se-rich Sb_2Se_3 samples. The amount of N_2 adsorbed on the Sb-rich Sb_2Se_3 is greatly larger than that adsorbed on the Se-rich Sb_2Se_3. This indicates that the Sb-rich Sb_2Se_3 sample has a larger surface area than the Se-rich Sb_2Se_3 sample. This results is in consistent with the surface area data where the Se-rich Sb_2Se_3 shows a lower specific surface area of 4.71 m^2/g, while the Sb-rich Sb_2Se_3 possess larger specific surface area of 12.25 m^2/g. The S_{BET} increase of Sb-rich Sb_2Se_3 was attributed to the smaller size of Sb-rich Sb_2Se_3 with hollow sphere-like morphology, which was in consistent with the results of TEM images. The pure Sb_2Se_3 could be made by the hydrothermal method at 180 ^oC with the ratio of Sb/Se 1:1.5 for 10 h. Fig. S3 shows its XRD pattern. Fig 4S presents the catalytic hydrogenation property of *p*-nitrophenol over the pure Sb_2Se_3. The catalytic hydrogenation property of *p*-nitrophenol over the pure Sb_2Se_3 shows only about 56% from Fig. 4S. It could be concluded that the high catalytic activity arises from the formation of hollow Sb-rich Sb_2Se_3 microsphere with high adsorption ability towards *p*-nitrophenol. The high catalytic activity may arise from the synergistic effect of Sb and Sb_2Se_3 nanoparticles catalyst: (1) the high adsorption ability of Sb_2Se_3 towards *p*-nitrophenol, providing a high concentration of *p*-nitrophenol near to the Sb nanoparticles on Sb_2Se_3; and (2) electron transfer from Sb_2Se_3 to Sb nanoparticles, facilitating the uptake of electrons by *p*-nitrophenol molecules, which leads to the reduction of *p*-nitrophenol into the *p*-aminophenol products. More investigations about the mechanism of the catalytic hydrogenation of *p*-nitrophenol over Sb-rich Sb_2Se_3 catalyst are needed in future work.

4. Conclusions

The Sb-rich Sb_2Se_3 catalyst has been successfully obtained under hydrothermal condition by adjusting the Sb/Se atomic ratio and reaction time. The Sb-rich Sb_2Se_3 is composed of hollow microsphere particles, while the Se-rich Sb_2Se_3 consists of short rod structure with smooth surface. Moreover, the as-prepared hollow Sb-rich Sb_2Se_3 products show more efficient catalytic performance than Se-rich Sb_2Se_3 for the reduction of *p*-nitrophenol to *p*-aminophenol at room temperature. These results indicate that the obtained hollow microsphere Sb-rich Sb_2Se_3 materials have the great potential for catalytic applications.

Acknowledgements

This research was financially supported by the National natural Science Foundation of China (No. 51374250) and Hunan Provincial Natural Science Foundation for Innovative Research Groups (No. 2013-2). We thank Ph.D. Yang Bai and Liang Zhou for assistance with BET measurements.

Notes and references

1. S. S. Zhang, J. M. Song, H. L. Niu, C. J. Mao, S. Y. Zhang and Y. H. Shen, *J Alloy Compd*, 2014, 585, 40-47.
2. T. T. Ngo, S. Chavhan, I. Kosta, O. Miguel, H. J. Grande and R. Tena-Zaera, *Acs Appl Mater Inter*, 2014, 6, 2843-2848.
3. H. M. Yang, M. Li, L. J. Fu, A. D. Tang and S. Mann, *Sci Rep-Uk*, 2013, 3.
4. X. C. Zhang and A. D. Tang, *Mater Express*, 2012, 2, 238-244.
5. N. Guijarro, T. Lutz, T. Lana-Villarreal, F. O'Mahony, R. Gomez and S. A. Haque, *J Phys Chem Lett*, 2012, 3, 1351-1356.
6. S. Messina, M. T. S. Nair and P. K. Nair, *J Electrochem Soc*, 2009, 156, H327-H332.
7. R. C. Jin, G. Chen, H. M. Xu and D. H. Chen, *Int J Hydrogen Energ*, 2013, 38, 10971-10977.
8. R. C. Jin, G. Chen, Q. Wang, J. X. Sun and Y. Wang, *J Mater Chem*, 2011, 21, 6628-6635.
9. X. Wang, K. F. Cai and H. Liu, *Cryst Growth Des*, 2011, 11, 4759-4767.
10. P. M. Kulal, D. P. Dubal and V. J. Fulari, *J Mater Sci*, 2011, 46, 2789-2795.
11. L. Guo, G. B. Ji, X. F. Chang, M. B. Zheng, Y. Shi and Y. D. Zheng, *Nanotechnology*, 2010, 21.
12. Y. Q. Liu, M. Zhang, F. X. Wang and G. B. Pan, *J Mater Chem C*, 2014, 2, 240-244.
13. R. C. Jin, G. Chen, C. S. Yan, D. H. Chen, H. M. Xu and J. Pei, *Crystengcomm*, 2012, 14, 8547-8553.
14. R. C. Jin, G. Chen, J. Pei, J. X. Sun and Y. Wang, *Nanoscale*, 2011, 3, 3893-3899.
15. J. M. Ma, Y. P. Wang, Y. J. Wang, Q. Chen, J. B. Lian and W. J. Zheng, *J Phys Chem C*, 2009, 113, 13588-13592.
16. S.-P. Sun and A. T. Lemley, *Journal of Molecular Catalysis A: Chemical*, 2011, 349, 71-79.
17. A. A. Ismail, A. Hakki and D. W. Bahnemann, *Journal of Molecular Catalysis A: Chemical*, 2012, 358, 145-151.
18. B. Lai, Y.-H. Zhang, R. Li, Y.-X. Zhou and J. Wang, *Chem Eng J*, 2014, 249, 143-152.
19. X. C. Zhou, X. H. Zhu, J. W. Huang, X. Z. Li, P. F. Fu, L. X. Jiao, H. F. Huo and R. Li, *Rsc Adv*, 2014, 4, 33055-33061.
20. M. Goepel, M. Al-Naji, P. With, G. Wagner, O. Oeckler, D. Enke and R. Gläser, *Chem Eng Technol*, 2014, 37, 551-554.
21. J. Li, C. Y. Liu and Y. Liu, *J Mater Chem*, 2012, 22, 8426-8430.
22. T. Ji, L. C. Li, M. Wang, Z. H. Yang and X. H. Lu, *Rsc Adv*, 2014, 4, 29591-29594.
23. G. F. Dang, Y. Shi, Z. F. Fu and W. T. Yang, *Chinese J Catal*, 2012, 33, 651-658.
24. H. M. Yang, K. Zhang, R. R. Shi, X. W. Li, X. D. Dong and Y. M. Yu, *J Alloy Compd*, 2006, 413, 302-306.
25. H. M. Yang, R. R. Shi, K. Zhang, Y. H. Hu, A. D. Tang and X. W. Li, *J Alloy Compd*, 2005, 398, 200-202.
26. B. Zhou and J. J. Zhu, *Nanotechnology*, 2009, 20, 085604.

